Folding Kinematics of Kirigami-Inspired Space Structures

Antonio Pedivellano[a,1], Sergio Pellegrino[a,*]

[a] *Graduate Aerospace Laboratories, California Institute of Technology, 1200 E California Blvd, Pasadena, 91125, CA, USA*

Abstract

This paper studies the folding of square, kirigami-inspired space structures consisting of concentrically arranged modular elements formed by thin shells. Localized elastic folds are introduced in the thin shells and different folding strategies can be obtained by varying the location of the folds and the sequence of imposed rotations. Modeling each modular element with rigid rods connected by revolute joints, numerical simulations of the kinematics of folding are obtained, including constraints that represent folding aids and a gravity offload system. These simulations are used to study two specific packaging schemes, and the folding envelopes of a specific structure are analyzed to identify the scheme that is easier to implement in practice. This particular scheme is demonstrated by means of a physical prototype.

Keywords: Deployable structures, Thin shells, Packaging, Kinematic analysis, Loop closure, Origami

1. Introduction

Origami, the japanese art of paper folding, and kirigami, the variant of origami that allows cuts as well as folds in the paper, have inspired novel

* Corresponding author

Email address: sergiop@caltech.edu (Sergio Pellegrino)

[1] Current address: DCubeD, Burgweg 6, 82110 Germering, Germany

deployable space structures that can be efficiently packaged for launch and built at low cost. Miura-ori (Miura, 1969; Miura and Pellegrino, 2020), a well-known example of an origami-based modular packaging concept, has led to the development of a novel deployable solar array (Miura and Natori, 1985). Other examples include packaging schemes for thin films in solar sails (Guest and Pellegrino, 1992; Furuya et al., 2011) and flexible panels in solar arrays (Zirbel et al., 2013) based on the concept of coiling a circular membrane around a central hub. Removal of localized buckles near the folds of a coiled membrane was achieved by allowing slip to occur along the folds (Arya et al., 2017).

These concepts have been extended to large deployable structures that will enable new space missions. An ongoing development is the ultralight, scalable structural architecture for the Caltech Space Solar Power Project (SSPP) (Arya et al., 2016), to provide square, flat structures that are tens of meters in size and can be tightly folded into a cylindrical envelope. A recent study (Brophy et al., 2022) has proposed a novel mission architecture to reach Uranus and Neptune using very large ultralight solar arrays that make it viable to use electric propulsion at great distances from the sun.

Large scale applications of this kind pose challenges beyond the existing origami research. Hence, the specific challenges that are addressed in the present study are related to the practical implementation of these folding schemes, achievable with only simple folding aids. In particular, it has to be ensured that no damage occurs during folding and that the self-weight of the structure is properly supported at all stages of folding.

The specific focus of the present paper is the Caltech SSPP structure schematically shown in Fig. 1a. It consists of bending-stiff trapezoidal modular elements, also denoted as “strips”, in a four-fold symmetric arrangement of concentric square loops. The strips are attached to four diagonal cords stretched between a central deployment mechanism and the tips of four deployable booms. The main structural elements of the trapezoids are thin-shell longerons placed along the longitudinal edges of the trapezoids, connected by transverse battens. Functional membranes, e.g., photovoltaic films and/or RF radiating elements, are attached to the strips. Localized elastic folds in the longerons allow compact packaging of these structures.

The packaging concept involves two steps, which are shown in Fig. 1b. The first is a folding step, in which each quadrant of the structure is z-folded to reach a star configuration. This step is followed by a coiling step in which the four arms of the star are coiled into a cylindrical configuration. Note that the folding step in Fig. 1b is different from Arya et al. (2016), as this initial study had demonstrated the packaging concept with only thin films, without considering relatively stiff structural elements.

The present paper studies the folding step through general numerical simulations, with the objective of considering practically important effects, such as the choice of constraints that provide support against self-weight, and using easily implementable folding aids. Folding is very important to the maturation of the overall structural concept, particularly because the scope for exploring different folding strategies experimentally is limited by the extensive use of carbon-fiber reinforced composite materials, whose brittle behavior restricts the trial and error exploration feasible on physical models.

High-fidelity simulations, along the lines of Pedivellano and Pellegrino

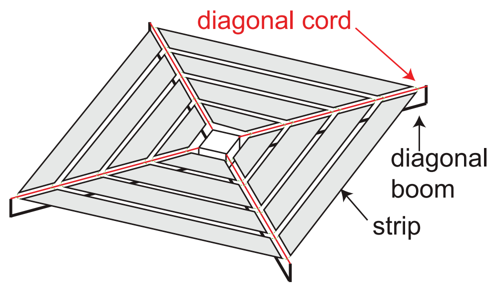

(a) Architecture

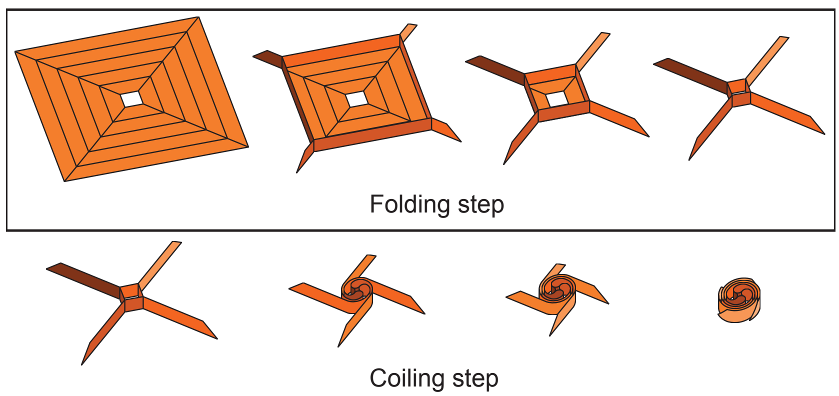

(b) Packaging scheme

Figure 1: Structural architecture and packaging concept, with the folding step highlighted.

(2022), might be thought as ideal for such studies. However, high-fidelity simulations are very time consuming and are best suited to the detailed analysis of specific folding problems.

Reduced-order finite element models offer a computationally efficient alternative to study elastic origami. A widely used approach is the bar-and-hinge method, which models a planar structure as an assembly of elastic bar elements forming a triangular pattern and revolute joints. Rotational springs along the bars model the behavior of the creases and fold lines (Filipov et al., 2017; Liu and Paulino, 2017). These models do a very good job in capturing the experimentally characterized behavior of deployable structures inspired by Miura-ori, including snap-through behavior.

Several authors have applied this method to the hypar, the origami pattern that is closest to the kirigami folding scheme studied in this paper. Filipov and Redoutey (2018) investigated the bi-stable behavior of the structure and showed that local and global buckling effects can be captured using this analytical method. Liu et al. (2019) focused on the geometric properties of the hypar and the tessellation of multiple hypar units to achieve multistability. The main weakness of the bar-and-hinge method is that, because it is based on an implicit finite element formulation, it struggles to deal with singularities in the tangent stiffness matrix, e.g. at bifurcation points. Liu et al. (2023) proposed an approach based on group theory to decompose the global formulation of a hexagonal hypar into a series of independent problems within different symmetry subgroups. This approach captured three different bifurcation branches of the equilibrium path during folding of the hypar, and examined the sensitivity of the corresponding peak loads to changes in the distance between the creases. In general, the bar-and-hinge method is not best suited to studying the motion of structures with a large number of kinematic paths. The complexity of this problem has been recognized in the physics literature, in which undesired kinematic paths are described as distractors (Stern et al., 2017).

The simulation approach adopted in the present study is focused on the specific structures of interest, which consists of long and narrow strips with localized elastic folds at specific, fixed locations, as shown in the box in Fig. 1b. The elastic folds and the strip-to-cord connections are modeled as hinges (revolute joints) and the remaining parts of the strips are modeled as rigid rods, hence modeling a complete structure as a mechanical linkage. With this approach, established analytical techniques for structural mechanisms can be used to develop an analytical framework to identify kinematically compatible paths for the structure. This formulation is then used to study different folding procedures, defined by the location of the imposed elastic folds and the order in which the square loops are folded.

The paper is organized as follows. Section 2 introduces a kinematic model of the structure where each strip is modeled as a linkage of rigid rods and revolute joints. Then, the whole structure is modeled by multiple closed loops, whose kinematics are simulated with a predictor-corrector algorithm. Section 3 studies the kinematics of a single square loop. Section 4 extends the single-loop solution to structures consisting of multiple, interconnected square loops. Section 5 presents an experimental demonstration of the best packaging scheme identified in the kinematic study. Finally, Section 6 discusses the results and concludes the paper.

2. Kinematic Model and Simulations

Consider a linkage consisting of straight rigid rods connected by revolute joints. A local reference frame is assigned to link i, see Fig. 2, with the origin O_i, x_i, y_i, z_i at one end, the z_i-axis aligned with the axis of the hinge, the x_i-axis in the plane defined by the z_i-axis and the axis of the link, and the y_i-axis chosen such as to form a right-handed reference frame.

Using the Denavit and Hartenberg (1955) notation, the reference frame for the next link, $i+1$, is related to the frame for link i by:

$$O_i = T_i O_{i+1} \tag{1}$$

where the 3D coordinates of point $\tilde{O}_i$ are transformed to the 4×1 extended form:

$$O_i = \begin{bmatrix} \tilde{O}_i \\ 1 \end{bmatrix} \tag{2}$$

Also,

$$T_i = \begin{bmatrix} R_i & v_i \\ 0_{1\times 3} & 1 \end{bmatrix} \tag{3}$$

where R_i, v_i are respectively a rotation matrix and a translation vector.

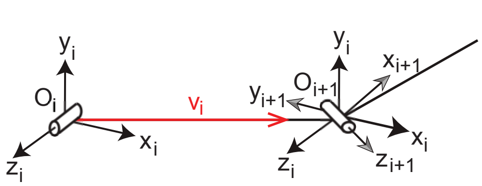

(a) Translation v_i of $x_i y_i z_i$ to the origin of $x_{i+1} y_{i+1} z_{i+1}$

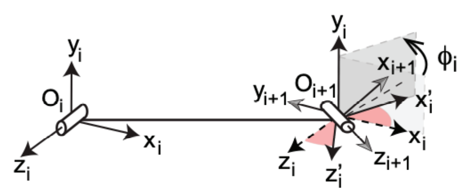

(b) Rotation ϕ_i about y_i-axis, such that z_i' lies in $y_i - z_{i+1}$ plane

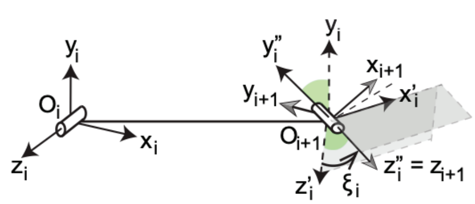

(c) Rotation ξ_i about x_i' to align z_i'' with z_{i+1}

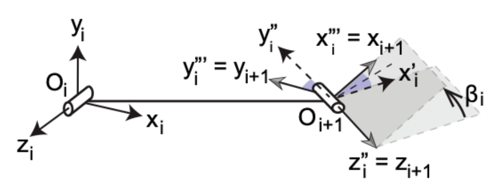

(d) Rotation β_i about z_i'' to align x_i''' with x_{i+1}

Figure 2: Coordinate transformations between local reference frames on adjacent links connected by a hinge.

The rotation matrices are defined in terms of three Euler angles, obtained from a sequence of elementary transformations that align the i-th reference frame with the $(i+1)$-th frame. The following convention is used:

1. translation v_i of the coordinate system from O_i to O_{i+1} (Fig. 2a);
2. rotation about the y_i axis by ϕ_i, until the rotated z_i'-axis is contained in the y_i-z_{i+1} plane (Fig. 2b);
3. rotation about the new x_i' axis by ξ_i, until the rotated z_i'' axis is aligned with z_{i+1} (Fig. 2c);
4. rotation about the $z_i'' = z_{i+1}$ axis by β_i, until x_i''' is aligned with x_{i+1} (Fig. 2d).

With this convention, ϕ_i is the angle between the $(i+1)$-th hinge axis and the normal to the i-th link axis; ξ_i is the twisting angle between the ends of the i-th link, and β_i is the fold angle, i.e., the rotation around the $(i+1)$-th hinge axis.

Coordinate transformations between non-consecutive links can be obtained by multiplying the transformation matrices of the links in between:

$$T_1^k = T_1 T_2 ... T_{k-1} \tag{4}$$

For a closed-loop kinematic chain, the initial and final coordinate frames must coincide, which is equivalent to the condition:

$$T_1 \; T_2 ... T_{n-1} T_n = I_{4\times 4} \tag{5}$$

This matrix equation provides the loop-closure constraint for a kinematic chain with n links. Although Eq. (5) corresponds to sixteen scalar equations, only six equations are linearly independent, and it is shown in Gan and

Pellegrino (2006) that an independent set of equations can be obtained from the six off-diagonal terms above the main diagonal.

Finding a kinematic path for the linkage requires finding a solution of Eq. (5). However, analytical solutions of this system of trigonometric equations are possible only for linkages much simpler than those considered in the present paper. Therefore, Eq. (5) was solved numerically, using the continuation algorithm proposed in Gan and Pellegrino (2006). This algorithm traces the motion of linkages with one or more degrees of freedom and identifies potential path-switching configurations (also known as kinematic bifurcations (Kumar and Pellegrino, 2000)) with a predictor-corrector algorithm that carefully monitors the approach to bifurcation points.

The incremental solution of Eq. (5) is based on a two-step algorithm. In the predictor step, the loop-closure equations are linearized to find kinematically admissible tangent motions and an increment of the solution is computed; in the corrector step, the linear prediction is iteratively updated until the error resulting from the linearization becomes smaller than a set threshold. These steps are outlined next.

2.1. Predictor step

Let C_i be the current configuration of the linkage, defined by the m variables $x_1, x_2, \dots x_m$.

In the predictor step, the loop-closure equation, Eq. (5), is linearized near C_i to obtain:

$$A_1 \Delta x_1 + A_2 \Delta x_2 + ... + A_{m-1} \Delta x_{m-1} + A_m \Delta x_m = 0_{4\times 4} \qquad (6)$$

where each of the coefficients A_j is the 4×4 matrix:

$$A_j = \Big(T_{1,j}|_{C_i} \, ... T_n(x_i) \Big) + ... + \Big(T_1(x_i) ... \, T_{n,j}|_{C_i} \Big) \tag{7}$$

Here, i denotes the time increment and $j \in [0, m]$ refers to the components of the state vector x. Partial derivatives of the transformation matrices have been denoted as $T_{i,j} = \partial T_i / \partial x_j$.

Eq. (6) provides up to six linearly independent scalar equations which, as previously discussed, are obtained from the six terms above the main diagonal of the matrix equation:

$$\begin{bmatrix} A_1^{(1,2)} & A_2^{(1,2)} \dots A_{m-1}^{(1,2)} & A_m^{(1,2)} \\ A_1^{(1,3)} & A_2^{(1,3)} \dots A_{m-1}^{(1,3)} & A_m^{(1,3)} \\ A_1^{(2,3)} & A_2^{(2,3)} \dots A_{m-1}^{(2,3)} & A_m^{(2,3)} \\ A_1^{(1,4)} & A_2^{(1,4)} \dots A_{m-1}^{(1,4)} & A_m^{(1,4)} \\ A_1^{(2,4)} & A_2^{(2,4)} \dots A_{m-1}^{(2,4)} & A_m^{(2,4)} \\ A_1^{(3,4)} & A_2^{(4,4)} \dots A_{m-1}^{(3,4)} & A_m^{(3,4)} \end{bmatrix} \begin{bmatrix} \Delta x_1 \\ \Delta x_2 \\ \vdots \\ \Delta x_{m-1} \\ \Delta x_m \end{bmatrix} = \begin{bmatrix} 0 \\ 0 \\ 0 \\ 0 \\ 0 \\ 0 \end{bmatrix} \tag{8}$$

This equation can be written in compact form as:

$$A_p \Delta x = 0 \tag{9}$$

The matrix A_p is the Jacobian of the system and the subscript p stands for predictor.

Non-trivial solutions of Eq. (9) belong to the null space of A_p, and can be obtained from the Singular Value Decomposition (SVD) of this matrix (Pellegrino, 1993; Golub and Van Loan, 2013). This decomposition computes three matrices U, V, and S such that

$$A_p = USV^T \tag{10}$$

where U and V are orthogonal matrices containing the left- and right-singular-vectors, with $U \in \mathrm{I\!R}^{6\times 6}$ and $V \in \mathrm{I\!R}^{\mathrm{m}\times\mathrm{m}}$, whereas S is a $6 \times m$ matrix containing the singular values.

For pin-jointed structures, Pellegrino (1993) has shown that the columns of V, corresponding to the null singular values, constitute a basis for the space of inextensional mechanisms of the structure. Analogously, in the present case, the columns of V identify a basis for the space of infinitesimal configuration changes that do not violate the loop-closure equation.

Denoting this basis with $\tilde{V}$, the predicted configuration of the linkage is:

$$x_p = x_i + \tilde{V}\alpha \tag{11}$$

where α is a vector of scaling parameters for the independent inextensional mechanisms that define the amplitude of the increment.

Note that, in the case of multiple mechanisms, a specific kinematic path is followed during the entire simulation. The predictor algorithm calculates, at each iteration, the dot product between the old eigenvector and the new eigenvectors and picks the increment closest to the path in the previous iteration.

2.2. Corrector step

The above linearized prediction results in a small error in the loop-closure equation, which therefore is no longer satisfied exactly. Hence, the error matrix E is defined from:

$$T_1(x_p)\, T_2(x_p)...T_{n-1}(x_p)T_n(x_p) = I_{4\times 4} + E \tag{12}$$

Eq. (12) is linearized following the same approach as in Section 2.1. A correction to the state vector is computed by defining the vector form of the error, $e = [E(1,2), E(1,3), E(2,3), E(1,4), E(2,4), E(3,4)]^T$, and then the correction is obtained from

$$A_c \Delta x = -e \tag{13}$$

where the subscript c stands for corrector.

A least squares solution of this equation can be computed with the SVD of A_c (Pellegrino, 1993; Kumar and Pellegrino, 2000):

$$\Delta x = -\sum_{i=1}^{\mathrm{rank(S)}} \frac{u_i^T \cdot e}{s_{ii}} v_i \tag{14}$$

where u_i and v_i are the left- and right-singular vectors of A_c, respectively.

The configuration of the linkage is updated with the correction:

$$x_c = x_p + \Delta x \tag{15}$$

and the correction step is repeated until the L2 norm of the error E (or any other metric of choice) becomes lower than a chosen tolerance, set to 10^{-9} in the algorithm. In a typical simulation, the error converges within two iterations of the correction step.

3. Folding a Loop of Four Strips

This section studies the folding kinematics of a square loop formed by strips of length $2L$ along the mid-line and width $2w$, Fig. 3. The strips are connected at the ends by hinges aligned with the diagonals of the square. According to the mobility formula for closed kinematic chains (Uicker et al., 2003; McCarthy and Soh, 2010), a closed loop requires at least seven revolute joints to have an internal degree of freedom. Therefore, at least three folds are needed and, in fact, four is the minimum number if folding is required to preserve the symmetry of the structure. However, the folding of nested loops requires at least two folds in each strip and hence this is the case considered here.

The non-dimensional parameter λ defines the distance between the folds. Note that $\lambda = 0$ corresponds to a single fold at the center of the strip, and $\lambda = 1$ corresponds to two folds at the ends. Since the folds are not allowed to cross the diagonal battens, the admissible range is $\lambda \in [0, \lambda_{max}]$ with:

$$\lambda_{max} = 1 - \frac{w}{L} \tag{16}$$

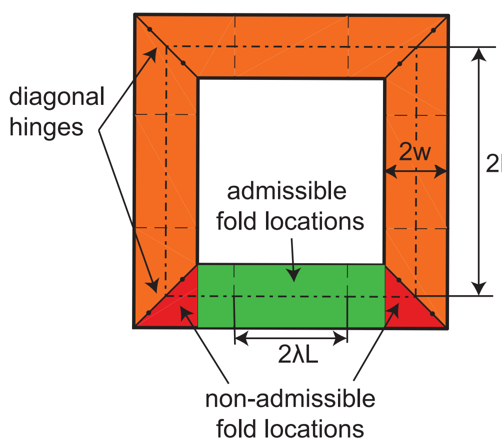

Figure 3: Geometry of square loop, with location of diagonal hinges and fold lines.

Figure 4 shows the model of the square loop. The joints have two rotational degrees of freedom around perpendicular axes, as shown in more detail in Fig. 5, and hence are equivalent to hinges with a variable direction axis. Hence, both bending β and torsion ξ of a strip are allowed. Therefore, the kinematic chain for the square loop contains $n = 12$ links with $m = 24$ degrees of freedom.

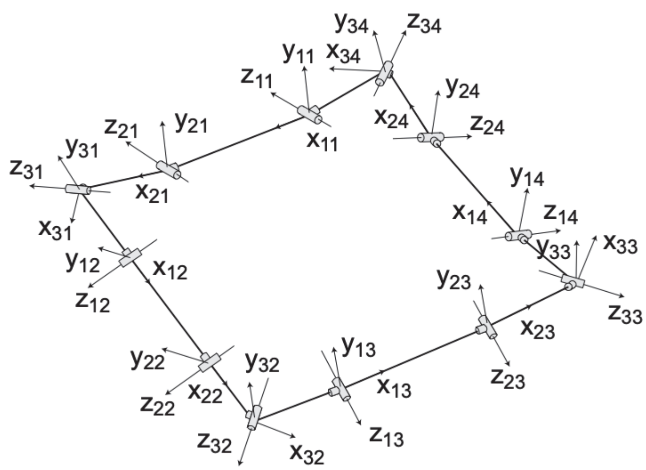

Figure 4: Kinematic chain of four strips forming a square loop.

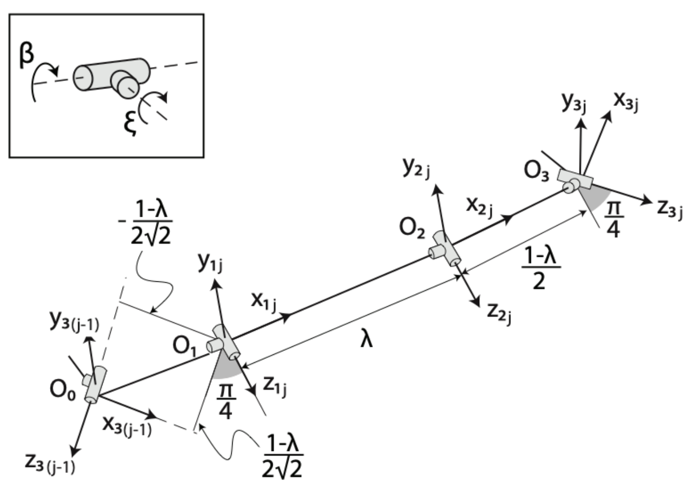

Figure 5: Detail of the kinematic model for a strip, with relevant dimensions.

A general strip j is shown in Fig. 5. The elementary transformations for this three-link model include the parameters β_{ij} and ξ_{ij}, corresponding to the degrees of freedom of the joints. The remaining (constant) parameters correspond to the geometry of the link and are provided in Table 1.

The angle ϕ_i is defined in Fig. 2b. Due to the four-fold symmetry of the structure, the rotation between the hinges and the folds is 45° for all of the strips (hinges and folds are defined in Fig. 3). The components of the translation vector only depend on the position of the folds. v_y is always zero, as the y_i-axis is perpendicular to the axis of the link, by construction. The distances in the model are non-dimensionalized by the length $2L$, so that the obtained results are valid for strips of any size.

	ϕ_i	v_x	v_y	v_z
T_{1j}	$\frac{\pi}{4}$	$\frac{1-\lambda}{2\sqrt{2}}$	0	$-\frac{1-\lambda}{2\sqrt{2}}$
T_{2j}	0	λ	0	0
T_{3j}	$\frac{\pi}{4}$	$\frac{1-\lambda}{2}$	0	0

Table 1: Denavit-Hartenberg parameters for the transformation matrices between adjacent links of a strip.

Once the transformation matrices have been defined, the loop-closure equation can be written in the form:

$$\prod_{j=1}^{4}\left(\prod_{i=1}^{3}T_{ij}\right)=I_{4\times 4} \tag{17}$$

and can be solved as described in Section 2.

Any configuration of this system is defined the vector $x \in \mathbb{R}^{24\times 1}$:

$$x=\begin{bmatrix}\beta_{11} & \beta_{21} & \beta_{31} & \beta_{12} & \dots & \beta_{34} & \xi_{11} & \xi_{21} & \xi_{31} & \dots & \xi_{34}\end{bmatrix}^T \tag{18}$$

In general, there are at least $24-6=18$ degrees of freedom, assuming that the Jacobian of Eq. (8) has full-rank. Solutions with specific symmetry properties can be obtained by introducing additional constraints.

3.1. Four-Fold-Symmetric Folding

Given that a square loop has four-fold symmetry, folding schemes that preserve this symmetry are of particular interest. This symmetry assumption greatly reduces the number of independent variables, by setting $\beta_{ij}=\beta_{i1}$ and $\xi_{ij}=\xi_{i1}\ \forall j \in [1,4]$. Symmetry also requires the folds on a strip to have the same angle ($\beta_{21}=\beta_{11}$) and prevents any torsion between their axes ($\xi_{21}=0$). It should be noted, however, that torsion is allowed between the hinges and the folds, under the constraint $\xi_{31}=-\xi_{11}$. Therefore, only three independent variables remain:

- β_{11}, denoted as the fold angle;
- β_{31}, denoted as the hinge angle;
- ξ_{11}, denoted as the torsion between the hinges and the folds.

With these constraints, the loop-closure equation and its linearized versions in Eq. (8), Eq. (9), Eq. (13), reduce to a system of 3 equations in 3 unknowns. The reduced Jacobian matrix, $\tilde{A}_p$, has rank 2 throughout the folding process, so that there is only one kinematically-admissible path between planar and folded configuration. Snapshots of the solution for four different values of the hinge angle β_{31} are shown in Fig. 6.

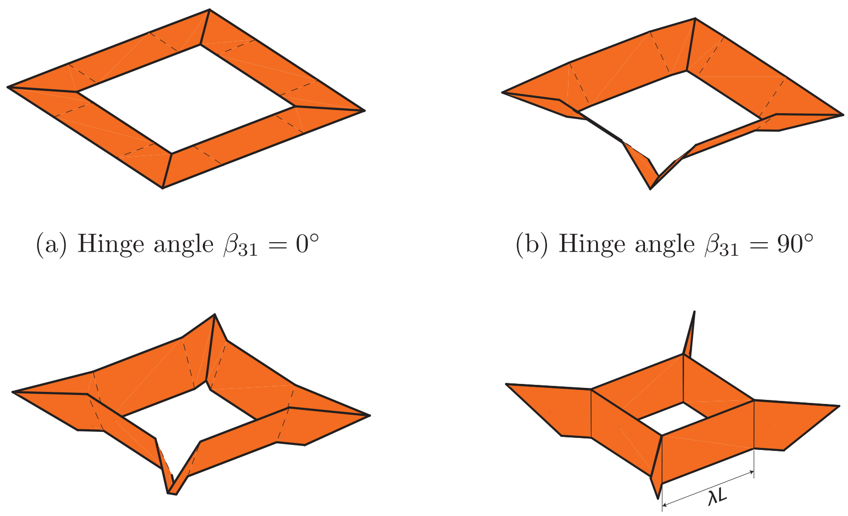

(a) Hinge angle $\beta_{31} = 0°$ (b) Hinge angle $\beta_{31} = 90°$

(c) Hinge angle $\beta_{31} = 135°$ (d) Hinge angle $\beta_{31} = 180°$

Figure 6: Four-fold symmetric folding of a loop of four strips.

Figure 7 shows the variation of the fold angle β_{11} and the strip torsion ξ_{11} with the hinge angle β_{31}. The plot shows that β_{11} monotonically decreases from 0° to -45° when the hinge angle is increased from 0° to 180°. The torsion of the strip ξ_{11} remains zero throughout the entire folding.

Figure 8 plots the variation of the singular values of $\tilde{A}_p$ as a function of β_{31}. One of the singular values is always equal to zero, indicating that there is a unique kinematic path. The other two singular values are greater

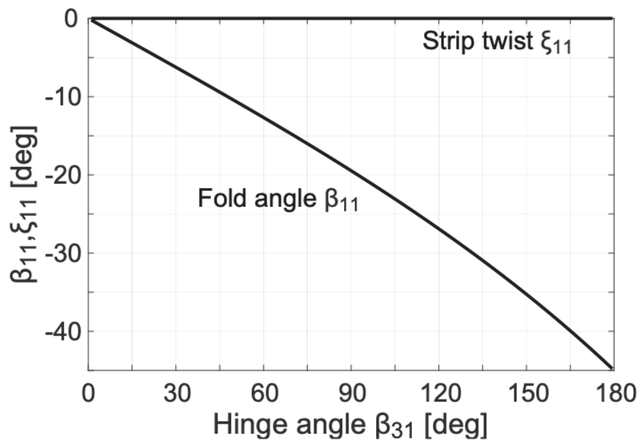

Figure 7: Four-fold-symmetric kinematic solution for single square loop.

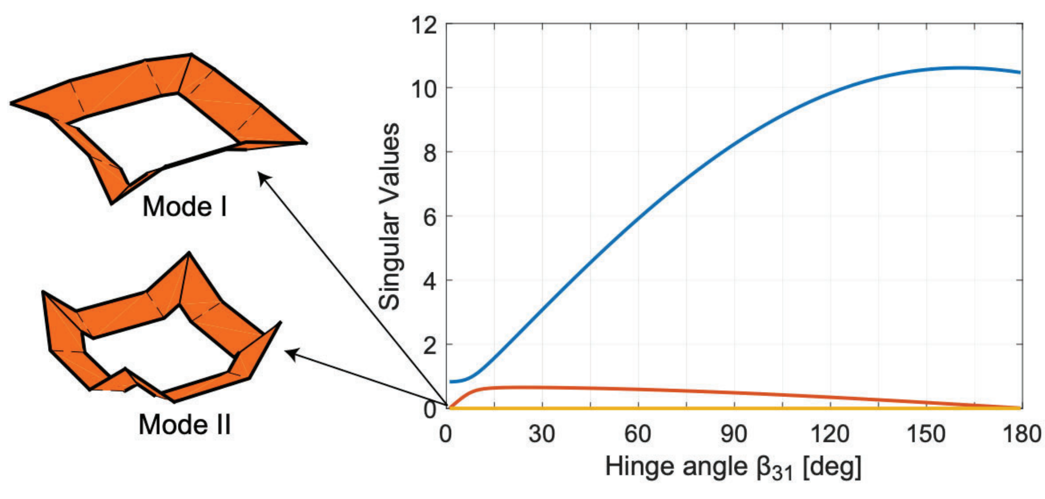

Figure 8: Singular values of $\tilde{A}_p$ along the four-fold-symmetric path. The two configurations shown on the left correspond to two different kinematic paths at the bifurcation point.

than zero for all values of β_{31}, except for the initial and final point ($\beta_{31} = 0$ and $\beta_{31} = 180°$), where the rank of $\tilde{A}_p$ drops to 1. This corresponds to a bifurcation point, at the intersection of two different kinematic paths. In the alternative folding path, the ends of the strips fold inwards, towards the center of the square, see Mode II in Fig. 8. To avoid the bifurcation, a small perturbation of 10^{-3} rad was applied to the initial configuration of the kinematic simulation.

The results in Fig. 7 were obtained for a fold spacing of $\lambda = 0.5$, but the results are identical for any other values of λ. This means that, although different values of λ correspond to different geometries of the structure, the relationship between the variables β_{11}, ξ_{11} and β_{31} remains unchanged.

The four-fold symmetric path considered in this section provides a single degree-of-freedom mechanism with torsion-free kinematics, which is beneficial for the structural integrity of the space structure. Therefore, it will used as the baseline for the packaging kinematics of a multi-square-loop structure in Sec. 4.

3.2. Folding with a Single Plane of Mirror Symmetry

The kinematic formulation presented in this paper can capture more general kinematic paths, which will be demonstrated by studying an alternative packaging strategy. A mirror symmetric folding scheme, in which a square loop is folded in two steps by moving two corners at a time, is shown in Fig. 9.

One of the outermost strips is folded first, by imposing 180° relative rotations at the end hinges. The rest of the structure follows in a symmetric fashion. Then, the opposite strip is folded in a similar way.

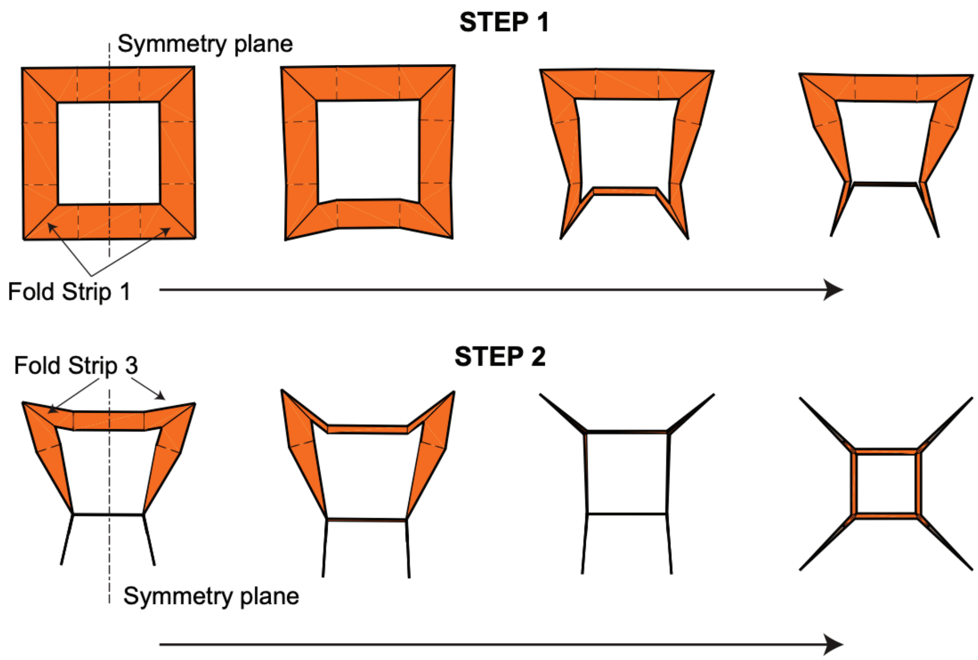

Figure 9: Mirror symmetric folding sequence for a square loop: corners C1 and C2 are folded first (strip 1), followed by corners (C3 and C4).

To model the kinematics of this folding scheme, the 24 variables in the general model of the square loop, Eq. 18 are reduced to only 11 by setting the following 13 symmetry conditions: for bending $\beta_{21} = \beta_{11}$, $\beta_{23} = \beta_{13}$, $\beta_{33} = \beta_{32}$, $\beta_{14} = \beta_{22}$, $\beta_{24} = \beta_{12}$, $\beta_{34} = \beta_{11}$, and for torsion $\xi_{21} = 0$, $\xi_{31} = -\xi_{11}$, $\xi_{23} = 0$, $\xi_{33} = -\xi_{13}$, $\xi_{14} = -\xi_{32}$, $\xi_{24} = -\xi_{22}$, $\xi_{34} = -\xi_{12}$. Hence, the reduced model includes only 11 degrees of freedom (6 bending rotations β_j and 5 torsional rotations ξ_j).

During the second folding step, β_{31} and ξ_{11} are set to zero to fix the folded corners of the square loop.

Under these assumptions, the linearized kinematics in Eq. 8 becomes underdetermined, as it has 6 equations and 11 unknowns. Eq. 11 provides a 5-dimensional space of solutions.

While arbitrary values of α would be kinematically feasible, practically useful solutions are obtained by solving the following optimization problem:

$$\alpha^* = \arg\min_{\alpha} J \tag{19}$$

in which $J = \sum_{i=1}^{3} w_i J_i$ and the weights w_i were all set equal to one in this particular case.

The cost function imposes the following practical requirements:

- $\mathbf{J_1}$ **: planarity.** During folding, the structure remains in contact with a planar surface, to offload gravity;
- $\mathbf{J_2}$ **: displacement.** The largest displacements (rotations) should correspond to the degrees of freedom being controlled;
- $\mathbf{J_3}$ **: torsion.** Torsional rotations should be as small as possible, to minimize the stress on the structure.

The condition J_1 is defined as follows:

- First, the coordinates of the lower longerons of the strip are evaluated at the joint locations, and expressed in their local frames ($P_i = [0, 0, -w, 1]^T$ at the elastic fold locations, $P_i = [0, 0, -\sqrt{2}w, 1]^T$ at the location of the hinges between strips, where the notation of Eq. (2) has been used.
- The coordinates P_i are converted to the same reference using the compound transformations $P_i^{(0)} = T_0^i P_i$;

- A global frame is defined, with the origin at the centroid O of the points $P_i^{(0)}$ and the axes aligned with the 0-th local frame. The global coordinates of the points were computed as $\overline{P}_i = P_i^{(0)} - O$;

- A plane passing through these points is defined, using the Principal Component Analysis (PCA) (Jolliffe, 2005) on the matrix $X = [P_1, P_2, \ldots P_n]$. The matrix contains the coordinates of the above defined points, 5 points on each longeron for a total of 20 points on the 4 longerons. The PCA returns the eigenvectors of the covariance matrix $X^T X$; the eigenvector corresponding to the smallest eigenvalue of $X^T X$ defines the normal n to the fitting plane.

- Finally, J_1 is defined as: $J_1 = \sum_i \left| \frac{\overline{P}_i}{\|\overline{P}_i\|} \cdot n \right|$.

The condition J_2 states that the displacement of the controlled D.o.F.'s should be larger than any other component, and hence

$$J_2 = 1 - \|x_c\| \tag{20}$$

where x_c is a vector containing the components of x_m associated with the control variables.

The condition J_3 minimizes the torsional components and is stated as:

$$J_3 = \| \, [\xi_{11}, ...\xi_{34}]\| \tag{21}$$

The optimization problem was solved using a quasi-Newton algorithm in MATLAB 2020, with the function `fminunc`. Fig. 10 shows the evolution of the bending and torsional degrees of freedom for the 2-step mirror symmetric folding path, on a strip with $\lambda = 0.5$.

In the first step, the control variable is β_{31}, which increases monotonically from 0° to 180°, while the fold angle β_{11} on strip 1 decreases to approximately $-90°$. The other bending angles vary by up to approximately 30°. Torsion is generally small, with the largest value corresponding to ξ_{22}, i.e. the twisting between the fold angles associated with strips 2 and 4.

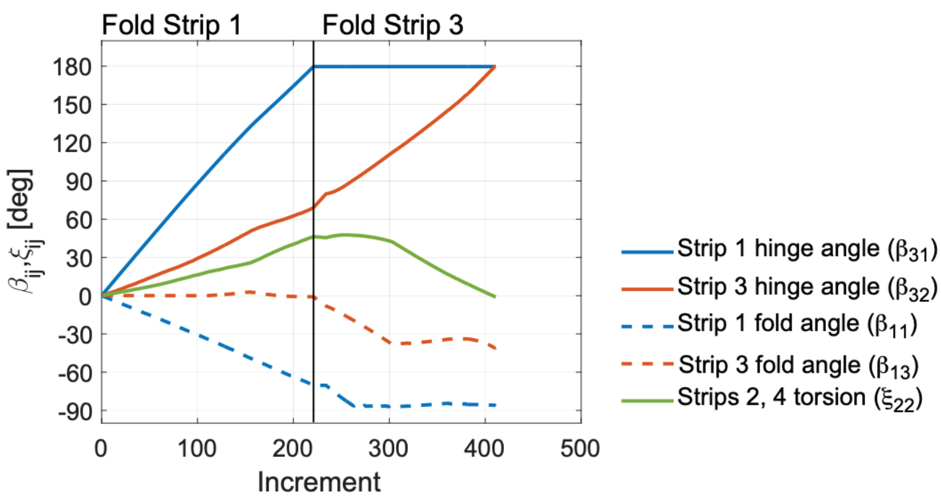

Figure 10: Two-step folding with a plane of symmetry.

These results show that it is possible to star-fold a square loop structure by controlling two degrees of freedom. Note that different kinematic paths controlled by two degrees of freedom are also possible.

4. Folding of Nested Square Loops

Section 3.1 has computed, for a single square loop, a four-fold-symmetric folding path with a single-degree-of-freedom. When multiple square loops are connected to form a nested space structure, the loops can be folded in sequence by ensuring that the loop kinematics are compatible.

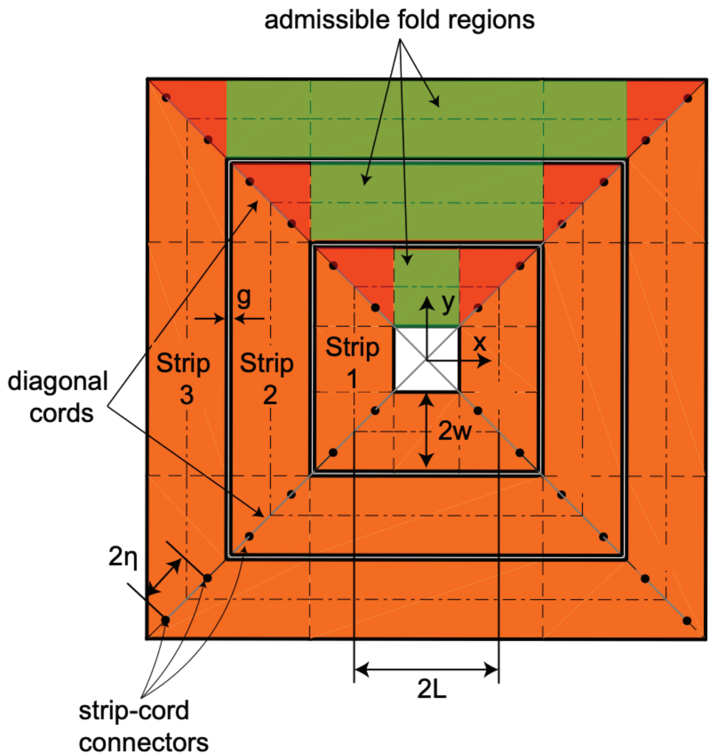

Figure 11: Geometry of structure consisting of three square loops. Each strip has two folds, symmetrically located with respect to the mid-plane.

A structure consisting of three square loops is shown in Fig. 11. Its geometry is defined by two non-dimensional parameters, the aspect ratio of the inner strip $\hat{w} = w/L_1$ and the non-dimensional joint spacing $\hat{\eta} = \eta/\sqrt{2}w$. There is in fact a third parameter, the gap between the strips, which is taken as $\hat{g} = g/w = 0$.

Unless otherwise specified, the results in this section assume $\hat{w} = 0.55$, $\hat{\eta} = 0.53$, and $\hat{g} = g/w \sim 0$, corresponding to the design of the physical prototype described in Section 5. Note that $2L_i$ is the length of the mid-line for the i-th square loop, while $2L = 2L_1$ refers to the innermost square loop and is the reference length used to nondimensionalize the results.

4.1. Sequential Folding

Each square can be folded using the four-fold-symmetric solution presented in Figs. 6 and 7. It corresponds to folding one loop at a time, starting from the outermost one and proceeding inwards, in sequence. In this case the location of the folds is constrained, as the loop being folded cannot interfere with the still flat (unfolded) loop inside it.

Specifically, during folding of the i-th loop, the shortest distance between opposite strips reduces from its original value of $2(L_i - w)$ to $2\lambda_i L_i$, as shown in Fig. 6. This distance cannot be smaller than the outer size of the next square loop, which is still fully deployed. Hence:

$$\lambda_i L_i \geq L_{i-1} + w \tag{22}$$

Therefore, the half-lengths L_i and L_{i-1} are related by the relationship:

$$L_{i-1} = L_i - 2w - g \tag{23}$$

and, substituting Eq. (23) into Eq. (22), the inequality can be solved for λ_i to obtain:

$$\lambda_i \geq \frac{L_i - w - g}{L_i} = 1 - \frac{w}{L_i} - \frac{g}{L_i} \tag{24}$$

where, as previously noted, $g/L_i = 0$ has been assumed.

Combining Eq. (24) with the constraint on λ, which avoids that the folds pass through the diagonal battens, Eq. (16), one finds that sequential folding is only possible if the folds are placed at the edges of their admissible regions, i.e., at the ends of the shortest longeron of the strips. Therefore, the folds are placed at these locations and the folding sequence in Fig. 12 is obtained.

At each step of the process, the next square loop is folded according to the four-fold-symmetric path derived in Section 3. However, there are some important additional considerations to make this work.

First, successive loops have to rotate in alternate directions, to avoid that the height of the packaged structure keeps increasing. This results in the z-folded arrangement shown in Fig. 13.

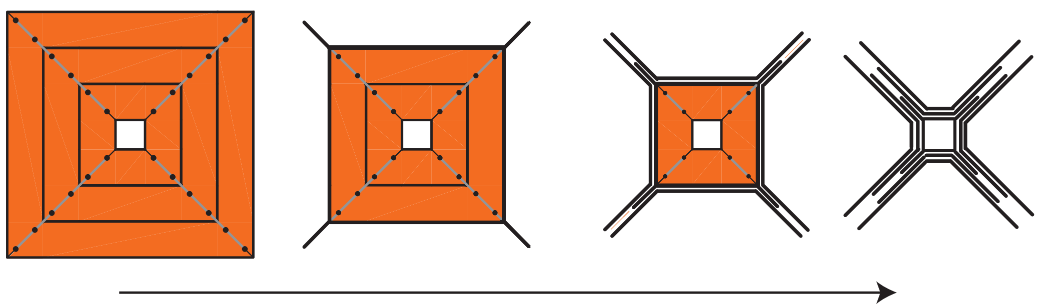

Figure 12: Folding sequence for a structure with 3 square loops that are folded one at a time (top view).

Second, previously folded loops have to be further deformed when the inner loops are folded, in order to push the strips towards the central square, as shown in Fig. 12. This involves additional folds in the already folded loops. The location of these folds has to match the folds of the loop that is currently being folded, as illustrated in Fig. 13a, where B indicates the initial fold location and A is the new fold location. A more detailed description of the kinematics is shown in Fig. 13b, which shows only half of the mid-line of the outer strip, for clarity.

Points B and C lie on the diagonal symmetry plane $x = y$, and hence

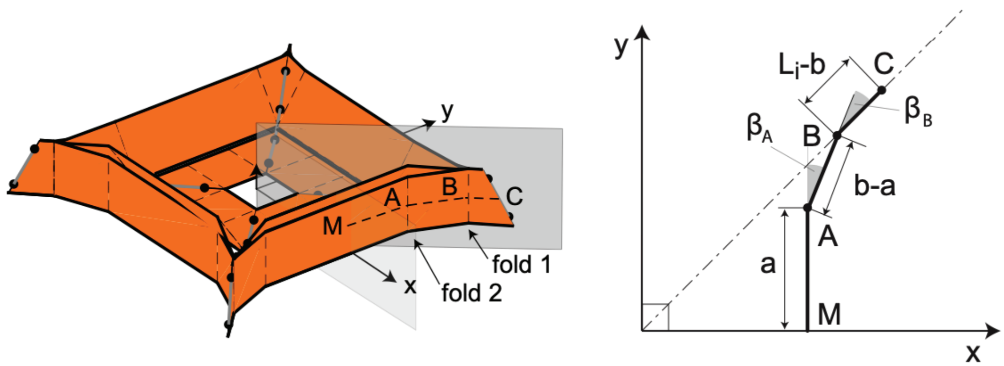

(a) Partially folded structure

(b) Top view

Figure 13: Formation of secondary fold A in strip with original fold B.

their coordinates are related by:

$$x_C = x_B + \frac{L_i - b}{\sqrt{2}} \tag{25}$$

The location of B is obtained by setting

$$AB = b - a \tag{26}$$

where a and b correspond to the distances between the symmetry plane of the strip and the two folds, measured along the strip mid-line. Eq. (26) can be expanded and rearranged as:

$$2x_B^2 - 2(x_A + a)x_B + x_A^2 + a^2 - (b - a)^2 = 0 \tag{27}$$

The solutions of this equation correspond to the two positions of B, on either side of A on the line $x = y$. The positive root is chosen.

Equations (25) and (27) contain three unknowns, x_A, x_B, and x_C. The first unknown, x_A, is chosen as a free parameter that controls the folding process. Its value decreases from $x_A = b$, corresponding to $\beta_B = 45°$ and

$\beta_A = 0°$, to $x_A = a$, corresponding to $\beta_B = 0°$ and $\beta_A = 45°$. In a simulation of the folding of multiple square loops, x_A can be chosen to match the corresponding point on the adjacent square loop, in order to achieve a tight packaging. This choice minimizes the distance between the loops during folding and also satisfies the distance constraints imposed by the diagonal cords connecting adjacent strips (shown in Fig. 1a).

An additional consideration is the relative vertical position of the loops, which is subject to the length constraints imposed by the diagonal cords, which are an additional structural element also described in Section 1. The vertical position of the loops depends strongly on the position of the strip-cord connectors, defined by the parameter η in Fig. 11.

Geometric considerations, based on Fig. 11, show that this parameter controls the length of the cord between adjacent strips through the relationship:

$$L_c = 2\sqrt{2}w(1 - \hat{\eta} + \frac{\hat{g}}{2}) \tag{28}$$

When $\hat{\eta} = 1$, i.e., the strip-cord connectors are located at the corners of the strips, the cord length reduces to $\sqrt{2}g$ and the adjacent corners of the strips are almost hinged to one another. On the other hand, when $\hat{\eta} = 0$, i.e., there is a single strip-cord connector at the center of the strips, the free length of the cord is at its maximum. Since the cords can be considered inextensible, the distance between the strip-cord connectors of adjacent strips cannot exceed the length of the cords at any stage of the packaging process. On the other hand, shorter distances can be accommodated by the cords becoming slack. Therefore, the following inequality must be satisfied:

$$(\Delta z)^2 + (\Delta s)^2 \leq L_c^2 \tag{29}$$

where Δs and Δz represent the in-plane and out-of-plane distances between adjacent strip-cord connectors at the ends of a given cord segment. Here, Δs can be obtained from the solution of the folding kinematics of the individual square loops, detailed in Section 3. Δz accounts for both the kinematics of the square loop being folded and the vertical offset imposed to the other square loops (folded in previous steps or still to be folded), in order to satisfy Eq. (29).

Imagine that the structure has been placed on a flat table (corresponding to $z = 0$) for packaging: because of gravity, each loop tends to move down towards the table. However, in some configurations, the cord length constraints do not allow the strip to reach the table, hence requiring the strip to be lifted by Δz_i.

Figure 14 shows a section of the structure at an intermediate step of such a folding process. It defines the offsets Δz_2 and Δz_1 for the middle loop (currently being folded) and the inner loop (still planar), respectively. The lower longeron of the external loop is initially located at $z = 0$.

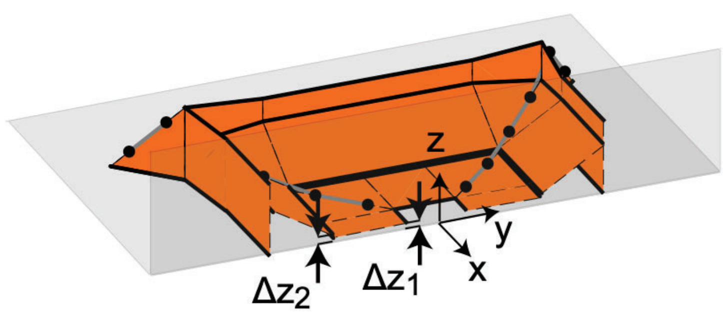

Figure 14: Vertical displacement of the strips from the plane $z = 0$.

The vertical offsets are defined as the smallest distances above the plane $z = 0$ for which the cord length constraints are satisfied. The calculation is performed for one loop at a time, starting from the external one and assuming the outermost edge remains in contact with the plane $z = 0$ (reference plane, corresponding to the table). This assumption is subsequently corrected if, after calculating the relative height changes between the strips, any of the strip heights are found to be negative (which would not be allowed by the presence of the table). In this case, the height of the point with the lowest value of z is set to zero, instead of the edge of the outermost strip.

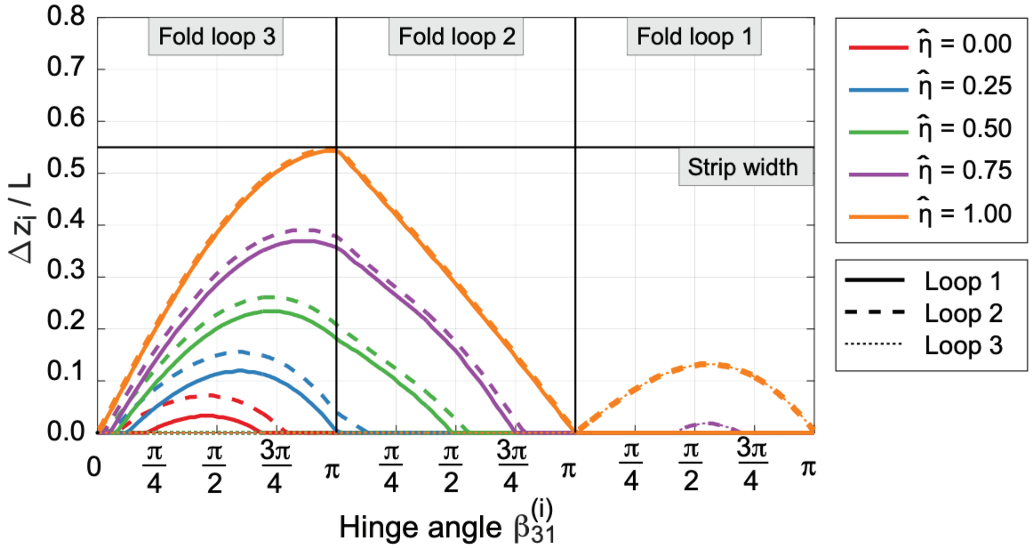

Figure 15: Vertical displacements of the strips for structure with three loops and joint spacing $\hat{\eta}$, folded one loop at a time.

Figure 15 shows the vertical offsets for a structure with three square loops and $\hat{w} = 0.55$, packaged by folding one loop at a time. At each folding step, the control parameter on the x-axis is the hinge angle of the loop currently being folded, $\beta_{31}^{(i)}$. Solid, dashed and dotted lines correspond to different loops, and results are shown for different values of the parameter $\hat{\eta}$.

For $\hat{\eta} = 1$, the inner corner of each square loop is coincident with the outer corner of the next inner loop. Therefore, during the first folding step, the upward motion of the inner corner of loop 3 leads to a vertical displacement of loops 2 and 1 by the same amount. When loop 3 is fully folded, both loops 2 and 1 are lifted from the reference plane by an amount equal to the width of the strips, while the outer edge of the structure remains in contact with the table ($\Delta z = 0$). In the second folding step, the outer edge of loop 2 remains at the same height, while the inner edge moves down as the fold angle of the strip increases. Loop 1, still parallel to the reference plane, follows the motion of the inner corner of loop 2. At the end of this step, $\Delta z_1 = \Delta z_2 = 0$. Next, the innermost loop is folded by lifting its inner edge. During this phase, the lowest point of the folded structure is the common edge between loops 1 and 2. While the outer edge of loop 1 moves up, the already folded loops 2 and 3 move together with it.

When $\hat{\eta}$ is decreased, the free length of the cord between adjacent square loops increases and provides some slack. This requires a smaller vertical displacement of loops 1 and 2 during the first folding step. The range of folding motion over which this displacement is required progressively decreases, and the peak displacement occurs at a smaller folding angle. A similar effect occurs during the third folding step. For $\hat{\eta} < 0.75$, loops 2 and 3 do not need to move up for loop 1 to fold.

Figure 15 also shows a second effect of the decrease in η. The required vertical displacement decreases as one moves away from the strip being folded. Specifically, in the first folding step (loop 3), the vertical displacement of strip 1 is consistently smaller than for loop 2.

4.2. Folding Loops in Pairs

The previous subsection has presented a scheme to fold the loops one at a time, starting from the outermost loop. Despite its conceptual simplicity, the practical implementation of this folding scheme is challenging due to the significant vertical offsets involved, as shown in Fig. 15. The kinematic analysis has shown that, at the end of the first step, the middle and inner loops need to be lifted from the plane $z = 0$, thus requiring a suspension system to offset gravity.

Hence, an alternative folding scheme is proposed, based on the idea of folding loops in pairs rather than individually. It will be shown that this scheme reduces the vertical offsets required during folding, and solves the problem of having to support the structure in between folding steps.

The intuitive argument is that the z-folding of concentric loops requires a sequence of alternating mountain and valley folds. When folding one loop at a time, the inner (planar) loops need to be coplanar with the mountain or valley folds, alternately. However, if the loops are folded in pairs, with a mountain fold in between them, the remaining loops can be coplanar with the valley folds.

The resulting two-step folding scheme is shown for a three-square-loop structure in Fig. 16. The outer and middle loops are folded first, and then the inner loop is folded.

In this case, the strips on the second and third loops must have folds at the same locations. This guarantees that, in their folded configuration, they will have the same size of the inner square. Hence, the location of the folds

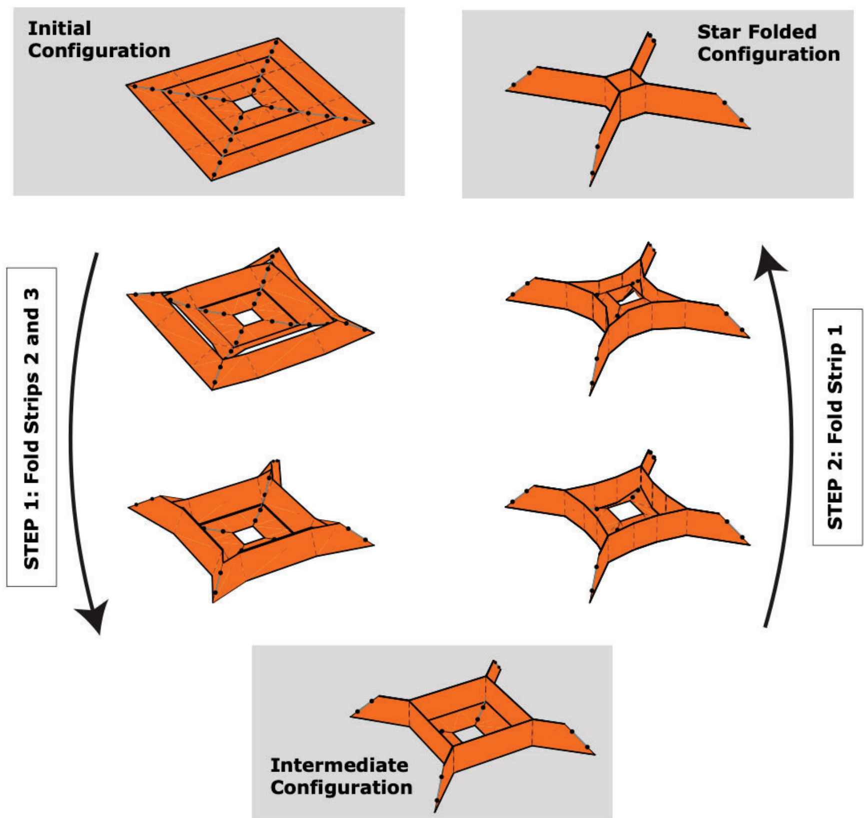

Figure 16: Two-step symmetric folding sequence for a structure with three square loops.

is defined by:

$$\lambda_2 = 1 - \frac{w}{L_2} \tag{30}$$

$$\lambda_3 = 1 - 3\frac{w}{L_3} \tag{31}$$

in order to satisfy the constraint $d_f = 2\lambda_2 L_2 = 2\lambda_3 L_3$.

Increasing the distance between the folds would place them in the non-admissible region for the middle loop, Fig. 11, while reducing the distance would result in an interference with the inner loop.

Figure 17 shows the required vertical offset Δz from the kinematic anal-

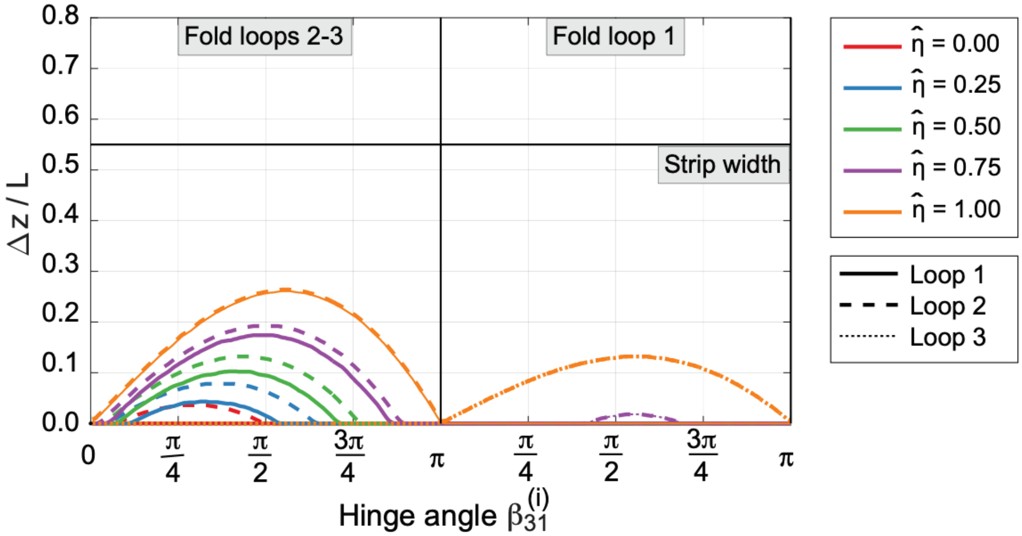

Figure 17: Vertical displacements of the loops for a structure with three loops folded in pairs and joint spacing $\hat{\eta}$.

ysis of this two-step folding scheme, as a function of the joint spacing $\hat{\eta}$. Similarly to the case shown in Fig. 15, the two-step folding scheme involves a vertical offset of loops 1 and 2 during the first folding step. The plot shows many of the features already observed in the previous case: the peak displacement is maximum when $\hat{\eta} = 1$ and progressively decreases when $\hat{\eta}$ is decreased. An offset between the vertical displacement of loops 1 and 2 is also observed during the first folding step, increasing in amplitude as $\hat{\eta}$ decreases. A key difference compared to the previous case is that, during the first folding step, loops 2 and 3 are folded simultaneously. Therefore, the maximum vertical displacement of loop 2 is approximately half of that predicted for the three-step folding scheme. More importantly, at the end of the first folding step, the vertical offset is zero for all loops and independent of $\hat{\eta}$. As an odd number of loops is considered for this example, the second and final step only requires folding of the innermost loop, which follows the same kinematics described for the three-step folding scheme in Fig. 15.

To understand how the maximum vertical offset changes with the size of the structure, the kinematic analysis was repeated for a structure with 10 loops, $\hat{w} = 0.55$ and $\hat{\eta} = 0.53$. In this case, there are five loop pairs and hence five folding steps are required. The required offsets are shown in Fig. 18, where pairs of loops folded together have been plotted with the same color. The figure shows that the maximum offset is the same for all of the steps, and has a value of about 13% of L, where L is the half-length of the innermost strip. During the first step, strip 10 remains on the plane $z = 0$, while loop 9 requires the largest vertical offset. The offset decreases as one moves inwards, with loops 1 to 4 requiring no offset at all.

A similar trend is observed for the other steps, in which the inner loop of the pair being folded always reaches the same maximum Δz and the four adjacent loops require a smaller offset. Additionally, the loops already folded need a small offset (with a maximum $\Delta z/L = 0.04$) too, when the hinge angle is in the range $\beta_{31}^{(i)} \in [3\pi/8, 3\pi/4]$.

The maximum Δz for structures folded in this way is independent of the number of loops, but only depends on the geometry of the strips, namely the parameters $\hat{w}$ and $\hat{\eta}$ defined in Fig. 11. The design space was explored to find the maximum Δz as a function of those parameters, and the results are shown in Fig. 19. This map shows that the offset increases both with the width of the strip and the spacing between the joints. In the case $\hat{w} = 1$, corresponding to a structure without a central hole, which is not practical, and $\hat{\eta} = 1$, Δz_{max} becomes about 42% of the innermost strip half-length, L.

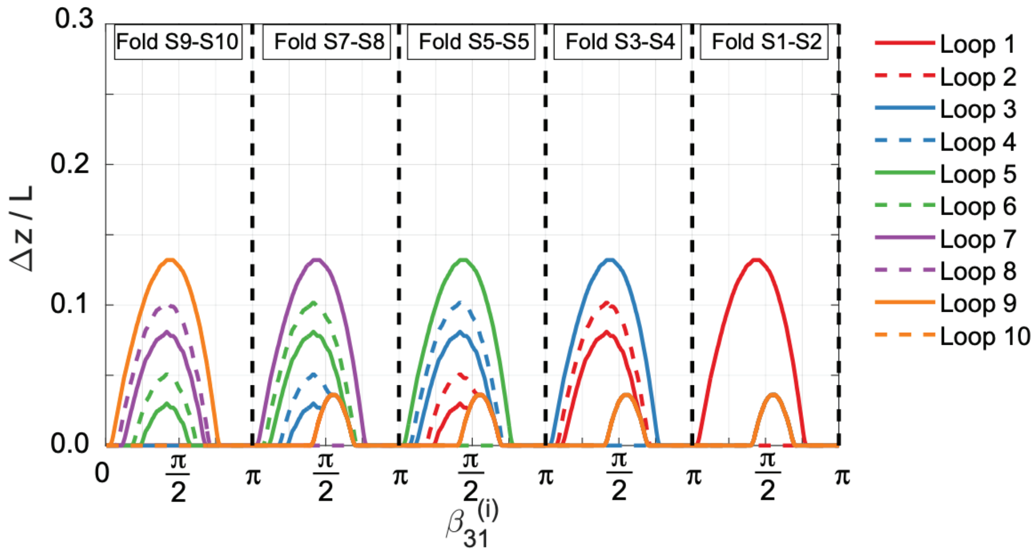

Figure 18: Vertical displacements of structure with 10 loops folded in pairs, $\hat{w} = 0.55$ and $\hat{\eta} = 0.53$.

The map also shows the design point for the structural prototype presented in Section 5, which has $\hat{w} = 0.55$ $\hat{\eta} = 0.53$.

5. Packaging Demonstration

The packaging scheme presented in Fig. 16 was demonstrated using a 1.7 m $\times$ 1.7 m prototype consisting of three 250 mm wide strips, placed on a flat table. Elastic folds were formed at the desired locations using hairpins to locally pinch each longeron. A two-step folding process was implemented, with the middle and outer loops folded first, followed by the inner one. At the end of each folding step, additional hairpins were added to hold together the folded strips.

For a structure of this size, two people were able to carry out the intended symmetric folding. While the kinematic simulation had assumed that the

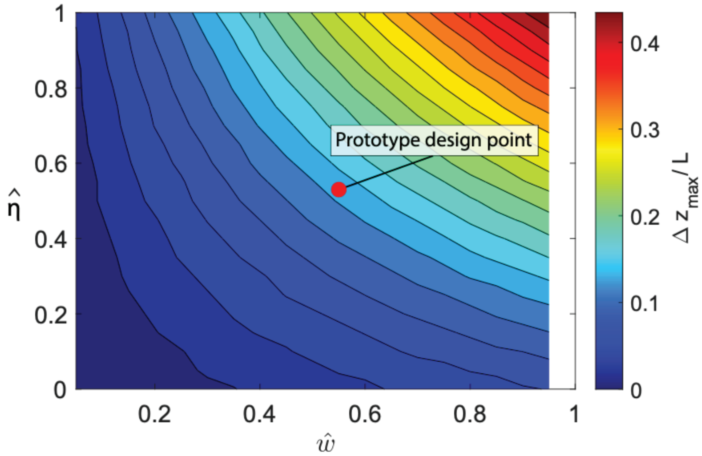

Figure 19: Maximum vertical displacement as a function of strip width $\hat{w}$ and joint spacing $\hat{\eta}$ for structures with any number of loops, folded in pairs.

control variable for the packaging process would be the end rotation of the strips, β_{3i}, in practice it was easier to fold the structure by pulling on selected control points. In particular, the first folding step was controlled by lifting the mountain fold between strips 2 and 3 at the location of the strip-to-cord connectors (red arrows in Fig. 20a), so that the strips would spontaneously rotate around the cord axes under the effect of gravity. In the second step, the shorter longerons of the inner strips were lifted, while the middle and outer strips, already folded, were pushed inwards until the structure reached the star configuration.

Figure 20 shows the packaging process, which closely resembles the prediction of the kinematic model (Fig. 16). The main deviation between the model and the physical implementation was in the location of the elastic folds for the first step. In particular, the model predicted the distance between the elastic folds should match the length of the shorter longeron on the second strip. In practice, this fold position resulted in a geometric interference with the inner square loop, as the actual width of the longeron cross-section on the middle square reduced the available space inside the folded loops. Therefore, the distance between the folds was increased by about 30 mm, so that the inner square could fit in between the others. A small amount of bending of the diagonal battens was then required, but the flexibility of the battens allowed such deformation without any difficulty or damage.

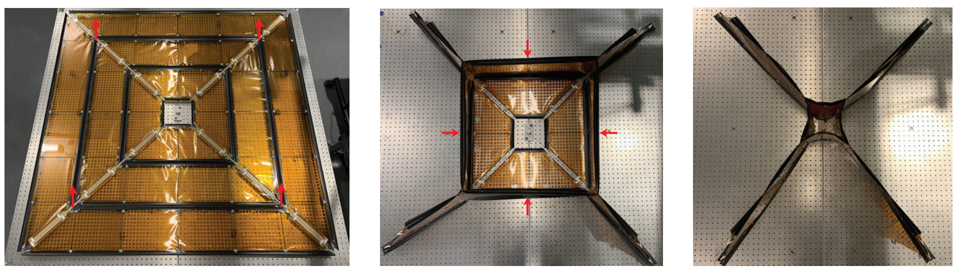

(a) Deployed (b) Loops 2 and 3 folded (c) Fully-folded

Figure 20: Packaging demonstration for 1.7 m×1.7 m prototype with 12 strips forming three square loops.

This successful demonstration has confirmed that the chosen kinematic sequence, developed through numerical simulations, allows a large structure to be folded without damage.

6. Discussion and Conclusion

This paper has presented and demonstrated the first study of kirigami-inspired space structures, considering the practicality of folding structures of large size, as well as the effects of self-weight, when designing the folding kinematics.

A kinematic approach to the problem of packaging space structures consisting of thin-shell strips of trapezoidal shape, arranged in concentric square loops and connected only through diagonal cords, has been presented. The strips have been modeled with rigid rods and revolute joints, making it possible to analyze a complete structure using tools that were previously developed for closed kinematic chains. Compatible kinematic paths for folding the structure have been identified, including a single-degree-of-freedom four-fold symmetric mechanism.

This approach allows folding of the structure in a predictable and repeatable way, reducing the risk of accidental damage. Although the range of deformations that can be applied to the thin-shell strips has been greatly restricted by the assumed symmetry, the required deformation could be simulated very efficiently. In fact, during the experimental demonstration described in Section 5, it has been found that, actually, these constrained symmetry-deformations can be easily implemented in practice.

The basic folding solution for a single loop undergoing four-fold symmetric folding, presented in Section 3.1, is defined by three rotations which, due to the symmetry assumption, have the unique relationship shown in Fig. 7. The analysis has revealed the existence of a kinematic bifurcation in the flat configuration of the strip, and hence careful control of the initial motion of the strip is required, to avoid that the strips set off on the wrong folding path. An alternative solution, that results in a packaging scheme with a single plane of mirror symmetry, has also been derived. It allows folding of a single loop structure by moving two corners at a time.

Using the basic solution for folding a single loop as a starting point, the folding of nested loops has been studied and two different approaches have been identified. In the first approach, the structure is folded sequentially, starting from the outermost loop and with the loops rotating in alternate directions. This approach requires the strip folds to be located at specific locations. As each strip is folded, the unfolded square region at the center of the partially packaged structure becomes gradually smaller. This requires the strip folds in previously folded strips to glide along the diagonals of the square structure, as highlighted in Figs. 12 and 13. In the second approach, the loops are folded in pairs, by synchronously rotating two consecutive loops in opposite directions and, again, starting from the outermost two loops. A significant advantage of this approach is that the vertical movement of the structure is greatly decreased.

An important constraint on the folding kinematics is imposed by the four diagonal cords to which the strips are attached. The constraints imposed by the cord lengths have been considered in Section 4, and an analysis of the boundary conditions on nested loops has revealed that the cords connecting adjacent strips require vertical translations to be applied to the strips during packaging.

For both folding approaches, the diagonal cord length constraints were included in the kinematic simulation and were used to calculate the minimum vertical translations required to fold the strips. It was found that, in both cases, shorter cords impose tighter constraints and increase the maximum vertical displacement during packaging. Folding the loops sequentially has been shown to require larger translations than folding the strips in pairs, as unfolded individual loops need to be alternately lifted from the folding table. On the other hand, folding the loops in pairs significantly reduces the required vertical displacements and ensures that, at the end of each folding step, all the loops lie on the folding table.

In conclusion, folding the strips in pairs appears to be the best way to package the structure in a sequence of simple steps, while minimizing the interaction between strips. It was also found that the design parameters of the space structure, i.e., the aspect ratio of the strips $\hat{w}$ and the spacing between strip-cord connectors $\hat{\eta}$, affect the kinematics of folding and their effect should therefore be taken into consideration in the early stages of the design process.

Acknowledgments

Financial support from the Space Solar Power Project (SSPP) at Caltech is gratefully acknowledged. The space structure prototype used in the present study was built by Eleftherios Gdoutos and Alan Truong.

References

Arya, M., Lee, N., Pellegrino, S., 2016. Ultralight structures for space solar power satellites, in: 3rd AIAA Spacecraft Structures Conference.

Arya, M., Lee, N., Pellegrino, S., 2017. Crease-free biaxial packaging of thick membranes with slipping folds. International Journal of Solids and Structures 108, 24–39.

Brophy, J., Pellegrino, S., Lubin, P., 2022. Non-Nuclear Exploration of the Solar System. Final Workshop Report for the W.M. Keck Institute for Space Studies, Pasadena, CA.

Denavit, J., Hartenberg, R.S., 1955. A kinematic notation for lower-pair mechanisms based on matrices. Trans. ASME , Journal of Applied Mechanics 22, 215–221.

Filipov, E.T., Liu, K., Schenk, M., Paulino, G.H., 2017. Bar and hinge models for scalable analysis of origami. International Journal of Solids and Structures, 124. 26–45..

Filipov, E.T., Redoutey, M., 2018. Mechanical characteristics of the bistable origami hypar. Extreme Mechanics Letters, 25. 16–26.

Furuya, H., Mori, O., Sawada, H., Okuizumi, N., Shirasawa, Y., Natori, M., Miyazaki, Y.,Matunaga, S., 2011. Manufacturing and Folding of Solar Sail “IKAROS”, in: 52nd AIAA/ASME/ASCE/AHS/ASC Structures, Structural Dynamics and Materials Conference 19th AIAA/ASME/AHS Adaptive Structures Conference, AIAA 2011-1967

Gan, W.W., Pellegrino, S., 2006. Numerical approach to the kinematic analysis of deployable structures forming a closed loop. Proceedings of the Institution of Mechanical Engineers, Part C: Journal of Mechanical Engineering Science 220, 1045–1056.

Gdoutos, E., Leclerc, C., Royer, F., Kelzenberg, M.D., Warmann, E.C., Espinet-Gonzalez, P., Vaidya, N., Bohn, F., Abiri, B., Hashemi, M.R., et al., 2018. A lightweight tile structure integrating photovoltaic conversion and rf power transfer for space solar power applications, in: 2018 AIAA Spacecraft Structures Conference.

Gdoutos, E., Leclerc, C., Royer, F., Türk, D.A., Pellegrino, S., 2019. Ultralight spacecraft structure prototype, in: AIAA SciTech Forum.

Gdoutos, E., Truong, A., Pedivellano, A., Royer, F., Pellegrino, S., 2020. Ultralight deployable space structure prototype, in: AIAA SciTech 2020 Forum.

Golub, G.H., Van Loan, C.F., 2013. Matrix Computations. JHU Press.

Guest, S.D., Pellegrino, S., 1992. Inextensional wrapping of flat membranes., in: Proceedings of the First International Seminar on Structural Morphology. University of Montpellier, IASS.

Jolliffe, I., 2005. Principal component analysis, in: Encyclopedia of Statistics in Behavioral Science (eds B.S. Everitt and D.C. Howell). https://doi.org/10.1002/0470013192.bsa501

Jones, P.A., Spence, B.R., 1998. Spacecraft solar array technology trends. IEEE Aerospace Conference Proceedings (Cat. No.98TH8339), 1998 Snowmass, CO, USA. IEEE, 141-152.

Kumar, P., Pellegrino, S., 2000. Computation of kinematic paths and bifurcation points. International Journal of Solids and Structures 37, 7003–7027.

Liu, K., Paulino, G.H., 2017. Nonlinear mechanics of non-rigid origami: an efficient computational approach. Proceedings of the Royal Society A: Mathematical, Physical and Engineering Sciences, 473. 20170348.

Liu, K., Tachi, T., Paulino, G.H., 2019. Invariant and smooth limit of discrete geometry folded from bistable origami leading to multistable metasurfaces. Nature Communications, 10. 4238.

Chen, Y., Xu, R., Lu, C., Liu, K., Feng, J., Sareh, P., 2023. Multi-stability of the hexagonal origami hypar based on group theory and symmetry breaking. International Journal of Mechanical Sciences, 247. 108196.

Mallikarachchi, H., Pellegrino, S., 2011. Quasi-static folding and deployment of ultrathin composite tape-spring hinges. Journal of Spacecraft and Rockets 48, 187–198.

McCarthy, J.M., Soh, G.S., 2010. Geometric Design of Linkages, second edition. Springer Science & Business Media.

Miura, K., 1969. Proposition of pseudo-cylindrical concave polyhedral shells. ISAS report/Institute of Space and Aeronautical Science, University of Tokyo, 34(9). 141-163.

Miura, K., Natori, M., 1985. 2-D array experiment on board a space flyer unit. Space Solar Power Review 5(4), 345–356.

Miura, K., Pellegrino, S., 2020. Forms and concepts for lightweight structures. Cambridge University Press.

Pedivellano, A., Pellegrino, S., 2021. Deployment dynamics of foldable thin shell space structures, in: AIAA Scitech 2021 Forum.

Pedivellano, A., Pellegrino, S., 2022. Deployment dynamics of thin-shell space structures. Journal of Spacecraft and Rockets 59, 1214-1227.

Pellegrino, S., 1993. Structural computations with the singular value decomposition of the equilibrium matrix. International Journal of Solids and Structures 30, 3025–3035.

Pellegrino, S., Gdoutos, E.E., Pedivellano, A., 2020. Actively controlled spacecraft deployment mechanism. US Patent App. 16/670,941.

Stern, M., Pinson, M.B., Murugan, A. 2017. The complexity of folding self-folding origami. Physical Review X, 7 (4). 041070.

Uicker, J.J., Pennock, G.R., Shigley, J.E., McCarthy, J.M., 2003. Theory of Machines and Mechanisms. Volume 768. Oxford University Press, New York.

Zirbel, S.A., Lang, R.J., Thomson, M.W., Sigel, D.A., Walkemeyer, P.E., Trease, B.P., Magleby, S.P., Howell, L.L., 2013. Accommodating thickness in origami-based deployable arrays. Journal of Mechanical Design, 135 (11). 111005.

Appendix A

The kinematic model described in Sec. 3 has been implemented in MATLAB 2020. It consists of two main scripts: the symbolic derivation and linearization of the loop closure equation, and its numerical solution through the corrector-predictor structure. They are reported in the following.

Derivation of the general loop closure equation

```
%------------------------------------------------------------
```

```
%Initialize symbolic variables and matrices
%------------------------------------------------------------
syms xi beta phi lams dx dz a syms xs11 xs21 xs31 xs12 xs22 xs32 xs13 xs23
xs33 xs14 xs24 xs34 syms bs11 bs21 bs31 bs12 bs22 bs32 bs13 bs23 bs33 bs14
bs24 bs34
    vars = ’bs11’,’bs21’,’bs31’,’bs12’,’bs22’,’bs32’,’bs13’,’bs23’,’bs33’,’bs14’,
’bs24’,’bs34’,’xs11’,’xs21’,’xs31’,’xs12’,’xs22’,’xs32’,’xs13’,’xs23’,’xs33’,’xs14’,
’xs24’,’xs34’;
    bs = [bs11, bs12, bs13, bs14; bs21, bs22, bs23, bs24; bs31, bs32, bs33,
bs34];
    xs = [xs11, xs12, xs13, xs14; xs21, xs22, xs23, xs24; xs31, xs32, xs33,
xs34];
    [dxs, dzs, ps] = deal(sym(zeros(3,4)));
%------------------------------------------------------------
%General formulation of the transformation matrix
%------------------------------------------------------------
    Rx = [1,0,0; 0, cos(xi), -sin(xi); 0, sin(xi), cos(xi)];
    Ry = [cos(phi), 0, sin(phi); 0,1,0; -sin(phi),0 , cos(phi)];
    Rz = [cos(beta), -sin(beta),0; sin(beta), cos(beta), 0 ; 0,0,1];
    RR = Ry*Rx*Rz; % Full rotation matrix
    Tg = [[RR, [dx; 0; dz] ]; 0, 0,0,1]; % Transformation matrix
%------------------------------------------------------------
%Specify known variables based on the geometry of the structure
% ------------------------------------------------------------
a = 0.5*(1-lams); % Location of the central fold
```

```
    ps(1,:) = pi/4;
    ps(3,:) = pi/4;
    dxs(1,:) = a/sqrt(2);
    dxs(2,:) = lams;
    dxs(3,:) = a;
    dzs(:) = 0;
    dzs(1,:) = -a/sqrt(2);
% -----------------------------------------------------------------
% Compute a matrix of symbolic transformation matrices
% -----------------------------------------------------------------
    % Ts is the complete transformation matrix for the loop
    % Tij is the transformation matrix between adjacent frames
    Tij = cell(3,4);
    Ttot = cell(3,4);
    for JJ = 1: 4
        for II =1: 3
            Tij{II,JJ} = subs(Tg,[phi, xi, beta, dx, dz],
                [ps(II,JJ), xs(II,JJ), bs(II,JJ), dxs(II,JJ), dzs(II,JJ)]);
        end
    end
% -----------------------------------------------------------------
% Transformation matrix for the whole loop
% -----------------------------------------------------------------
    TL = Tij{1,1} * Tij{2,1} * Tij{3,1} * Tij{1,2} * Tij{2,2} * Tij{3,2};
    TR = Tij{1,3} * Tij{2,3} * Tij{3,3} * Tij{1,4} * Tij{2,4} * Tij{3,4};
```

```
    Tt = TL*TR;
% Select elements of the matrices to use to enforce the loop-closure condition
    elements = [1,2; 1,3; 2,3; 1,4; 2,4; 3,4];
    % Write loop-closure equations
    fID = fopen('eqns.dat','w');
    for II = 1:6
    fprintf(fID,'f(%d) = %s;
n', II, Tt(elements(II,1),elements(II,2)));
    end
    fclose(fID);
    vars = {'bs11','bs21','bs31','bs12','bs22','bs32','bs13','bs23','bs33','bs14','bs24','bs34',
    'xs11','xs21','xs31','xs12','xs22','xs32','xs13','xs23','xs33','xs14', 'xs24', 'xs34'};
%===========================================
% CHOOSE MODEL
%===========================================
% CASE 1: symmetric folding
% CASE 2: sequential folding - C1
% CASE 3: sequential folding, C1 folded, fold C3
% CASE 4: sequential folding, C1 folded, fold C2
% CASE 5: sequential folding, C1 & C3 folded, fold C2
% CASE 6: sequential folding, C1 & C2 folded, fold C3
% CASE 7: sequential folding, C1 and C3 together
% CASE 8: sequential folding, C1 and C2 together
% CASE 9: sequential folding, C1 & C2 folded, fold C3
% CASE 10: sequential folding, C1 & C2 folded, fold C3 & C4
```

```
% CASE 11: sequential folding, all folded, make configuration symmetric
    [R2G, G2R, x_set_backup, control] = dof(1);
    [ ,j] = find(G2R);
    vars_red = vars(j); Nvars = length(vars_red);
%——————————————————————————————-
% TRANSFORMATION MATRIX FOR THE WHOLE LOOP
%——————————————————————————————-

    TL = Tij{1,1} * Tij{2,1} * Tij{3,1} * Tij{1,2} * Tij{2,2} * Tij{3,2};
    TR = Tij{1,3} * Tij{2,3} * Tij{3,3} * Tij{1,4} * Tij{2,4} * Tij{3,4};
    Tt = TL*TR;
    [var_old, var_new] = deal(sym([]));
    flag = false(24,1);
    for II =1:length(vars)
        Ai = R2G(II,:);
        % If the variable is used
        if any(Ai)
            xg = varsII;
            xr = vars_redAi =0;
            coeff = Ai(Ai =0);
            % If the variable depends on another variable
            if  strncmp(xg,xr,4)
                var_old(end+1) = eval(xg);
                var_new(end+1) = coeff * eval(xr);
            end
```

```
            else
                flag(II) = 1;
                if x_set_backup(II) ==0
                xg = varsII;
                var_old(end+1) = eval(xg);
                var_new(end+1) = x_set_backup(II);
            else
            end
        end
    end
    Tt = subs(Tt, var_old, var_new);
    % Compute derivatives wrt active variables
    for II =1: length(vars_red)
        Nij = diff(Tt,eval(vars_red{II}));
    end
    fclose(fID);
    % Numerical solution of loop closure equation
    lam = 0.75; w = 0.24; Nvars = length(vars_red);
    rankThreshold = 1e-3;
    threshold = 1e-6;
    errMax = 1e-9;
    maxIter = 10;
    maxInc = 300;
    amp = deg2rad(1); % Amplitude of angle increment
%==========================================
```

```
% INITIAL CONDITIONS
%==============================================

    x_set = x_set_backup;
    x0 = G2R*x_set;
    x_set( flag) = 0;
    x0(control) = x0(control) + 1e-3;
    [xcomp,err] = fsolve(@(x)loop_closure_gen(x,lam,R2G,x_set),x0);
    x0 = xcomp;
    KK = 0;
    [theta,beta,xi] = deal([]);
    eig = [];
    xsol = [];
    iter = [];
    error = [];
    fval = [];
    while abs(x0(control)) < pi && KK<maxInc
        KK = KK + 1;
        % Create linearized matrix
        x0g = R2G * x0 + x_set;
        N = Nred(x0g, lam);
        [U,S,V] = svd(N);
        eig(:,KK) = diag(S);
        r = rank(S,rankThreshold*max(diag(S)));
        m = Nvars - r;
```

```
% Choose increment
dirs = V(:,end-m+1:end);
if m>1
    cguess = zeros(m,1);
    ind = find(abs(dirs(control,:))==abs(max(dirs(control,:))));
    cguess(ind) = 1;
    w = [1,0,1,0,1]; % case 2
    w = [0,0,0,0,0]; % case 3;
    w = [1,0,0,0,10]; % case 4
    w = [1,100,0,0,10]; % case 6
    w = [0.05,0,1,1,0]; % case 10
    w = [1,1,1,1,1]; % case 11
    options = optimoptions('fminunc','MaxFunctionEvaluations',
    1e4,'algorithm','quasi-newton','optimalityTolerance',1e-9);
    [copt,fval(KK)] = fminunc(@(c)optim_dir(c,dirs,R2G,control,w,
    lam,x0g),cguess,options);
    dx = dirs*copt;
    dx = dx/vecnorm(dx);
else
    dx = dirs;
end
sgn = sign(dx(control));
xp = x0 + sgn * amp * dx;
iter(KK) = 0;
error(KK) = 1e3;
```

```
        while error(KK) >errMax && iter(KK)<maxIter
                iter(KK) = iter(KK)+1;
                xpg = R2G * xp + x_set;
                E = Tgen(xpg,lam) - eye(4);
                Np = Nred(xpg,lam);
                [Up, Sp, Vp] = svd(Np);
                F = E(1:3,1:3);
                f = (F - F')/2;
                e = [f(1,2); f(1,3); f(2,3); E(1:3,4)];
                r = rank(S, threshold);
                dxc = zeros(Nvars,1);
                for II = 1: r
                dxc = dxc - Vp(:,II) * Up(:,II)'/ Sp(II,II) * e;
            end
            xp = xp + dxc;
            error(KK) = max(abs(e));
        end
        x0 = xp;
        xsol(:,KK) = x0;
    end
    xsol(:,end) = [];
    theta = rad2deg(xsol(1,:)); beta = rad2deg(xsol(2,:)); xi = rad2deg(xsol(3,:));
```